Updated Performance Measurements and Analysis of the Phase Four RF Thruster

M. Umair Siddiqui* and Christopher Cretel†
Phase Four, El Segundo, CA, 90245

We present direct thrust, specific impulse, and thrust efficiency measurements of the next generation of electrodeless RF thrusters under development at Phase Four. Measurements were performed on torsional balance thrust stands at The Aerospace Corporation and at Phase Four. The experiments tested two thrusters, a low power CubeSat-optimized unit (35 W to 100 W RF power) and a higher power Small Sat-designed system (100 W to 500 W RF power). The thrusters generated between 0.3 and ≈ 9 mN of thrust (F_T), and between 61 and ≈ 1,500 seconds of specific impulse (I_{sp}) across that power range. The maximum thrust efficiency (η) measured was 10% ± 1%. To the authors' knowledge, these results represent the best electrodeless RF thruster direct measurements ever publicly disclosed.

I. Nomenclature

F_T	=	Thrust
g_0	=	Earth surface gravitational acceleration
I_{sp}	=	Specific impulse
$\dot{m}$	=	Mass flow rate
η	=	Thrust efficiency
P_{RF}	=	RF power

II. Introduction

The rise in standard, mass manufactured satellite buses is driving electric propulsion development to new technologies that are scalable in application, perform effectively, and are efficiently manufacturable in volume. While existing Hall effect thrusters and gridded ion engines perform extremely well and have over 40 years of test and flight heritage, they can be expensive to source and difficult to manufacture at scale [1]. Among the new technologies in development for such applications are electrodeless radio frequency (RF) thrusters. RF thrusters are electric propulsion systems that use radio frequency electromagnetic signals to ionize and excite a plasma as part of the propellant utilization process. "Electrodeless" RF thrusters are distinct from Hall effect thrusters, gridded ion engines, and gridded RF thrusters [2, 3] (such as the Ariane Radio frequency Ion Thruster) in that they do not use grids, anodes, cathodes, or high voltages to accelerate the propellant, greatly simplifying the thruster architecture. Their electrical and mechanical simplicity allows for electrodeless RF thrusters to be designed for the production requirements of the next generation of large satellite constellations.

Despite their promise, electrodeless RF thrusters have not gained wide acceptance due to their sub-par measured performance compared to state of the art Hall effect and gridded ion systems. Examples include the kW-scale VAriable Specific Impulse Magnetoplasma Rocket (VASIMR) [4], the ~ 500 W Helicon Double Layer Thruster (HDLT) [5], and various academic RF thrusters [6, 7]. Here we present direct thrust, specific impulse and thrust efficiency measurements of the Phase Four Radio Frequency Thruster (RFT). The Phase Four RFT approaches the concept of electrodeless RF plasma acceleration by acknowledging that the primary technological advantage of RF lies in the minaturazation of RF power electronics by the wireless power industry. Therefore, electrodeless RF thrusters and their power electronics are suited to miniaturization and volume manufacturing applications. Moreover, decreasing the plasma volume maximizes RF power density in the plasma, improving performance. Previously, proof-of-concept "RFT-0" measurements were presented which demonstrated that a rapidly designed small-scale RF thruster achieved thrust-to-power and thrust

*Chief Scientist, Phase Four, AIAA Senior Member.
†Propulsion Test Engineer, Phase Four, AIAA Member.

efficiencies greater than the RF thrusters tested at the Georgia Institute of Technology and at the University of Michigan, at comparable thrust and specific impulse levels [8]. In this paper we disclose direct thrust testing results of the next generation RF thrusters, including the CubeSat-class 40 W to 100 W "RFT-2" and the Small Sat-class 100 W to 500 W "RFT-X".*

III. The Phase Four Radio Frequency Thruster

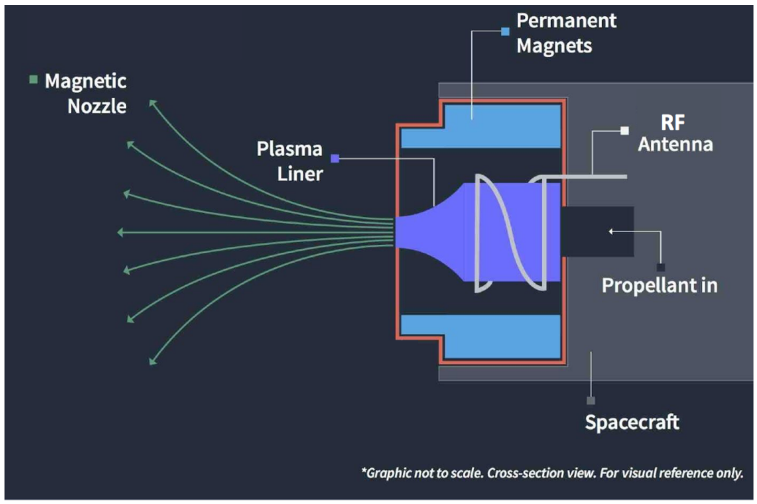

Fig. 1 A cross-sectional diagram of the core components of the Phase Four RFT family of thrusters.

Figure 1 shows a representative diagram of the Phase Four RFT. Gaseous propellant is injected into a "plasma liner", which is wrapped in a proprietary RF antenna. The entire assembly is housed inside a tailored magnetic field called the "magnetic nozzle". When an RF signal is applied to the antenna, the near-field pattern acts to ionize the propellant in the liner, and subsequently heat the plasma via stochastic electron-RF interactions [9, 10]. These interactions drive electrons out of the exit of the plasma liner. To maintain steady state charge balance, ions are accelerated by this momentary charge imbalance out of the liner, generating thrust. The proprietary magnetic field geometry acts to reduce plasma-wall losses, focus the fast electrons (and thus the ion beam), and impart a time-averaged bias to the directions in which fast electrons and ions outflow from the liner. It is important to note that the Phase Four RFT is *not* a "helicon" thruster. The helicon wave, a right-hand polarized electromagnetic wave that propagates in a plasma with a radial boundary along an axial magnetic field, plays no role in any substantial energy transfer in RFT plasmas. The scale sizes in RFT plasmas are too small to allow for meaningful RF heating to occur through any interactions with helicon waves or associated effects (such as Trivelpiece-Gould wave heating [11], parametric daughter wave heating [12], or Landau damping [13]).

The process is by definition and physical process, ambipolar, obviating the need for a cathode neutralizer. This advantage removes all high voltage electronics from the system. Furthermore the lack of electrodes allows the thruster to be used with a wide variety of propellants which may normally be corrosive to cathodes and anodes in the plasma state. Through experimentation and understanding of the primary plasma heating and loss mechanisms, Phase Four has developed a proprietary set of scaling laws and thruster component geometry relationships, to define thruster size and magnetic field strength for a specific power class of engine. The thrusters presented here, RFT-2 and RFT-X, while designed around different power applications, both follow the same set of design rules. Figure 2 shows images of the thrusters firing in the Phase Four VCH-1 "Dreadnought" vacuum facility.

IV. Experimental Setup

Figure 3 shows a line diagram description of the RFT control setup. For the measurements performed here, the engines under test were powered by laboratory class A broad band power amplifiers. The forward and reflected power to and from the thruster was monitored either by in line power meters or by internal amplifier monitoring circuitry, depending on the amplifier used (either an ENI or an IFI SCCX model). A bidirectional 200 W 50 dB coupler, 0.2

*These results do not represent Phase Four product specifications unless explicitly noted.

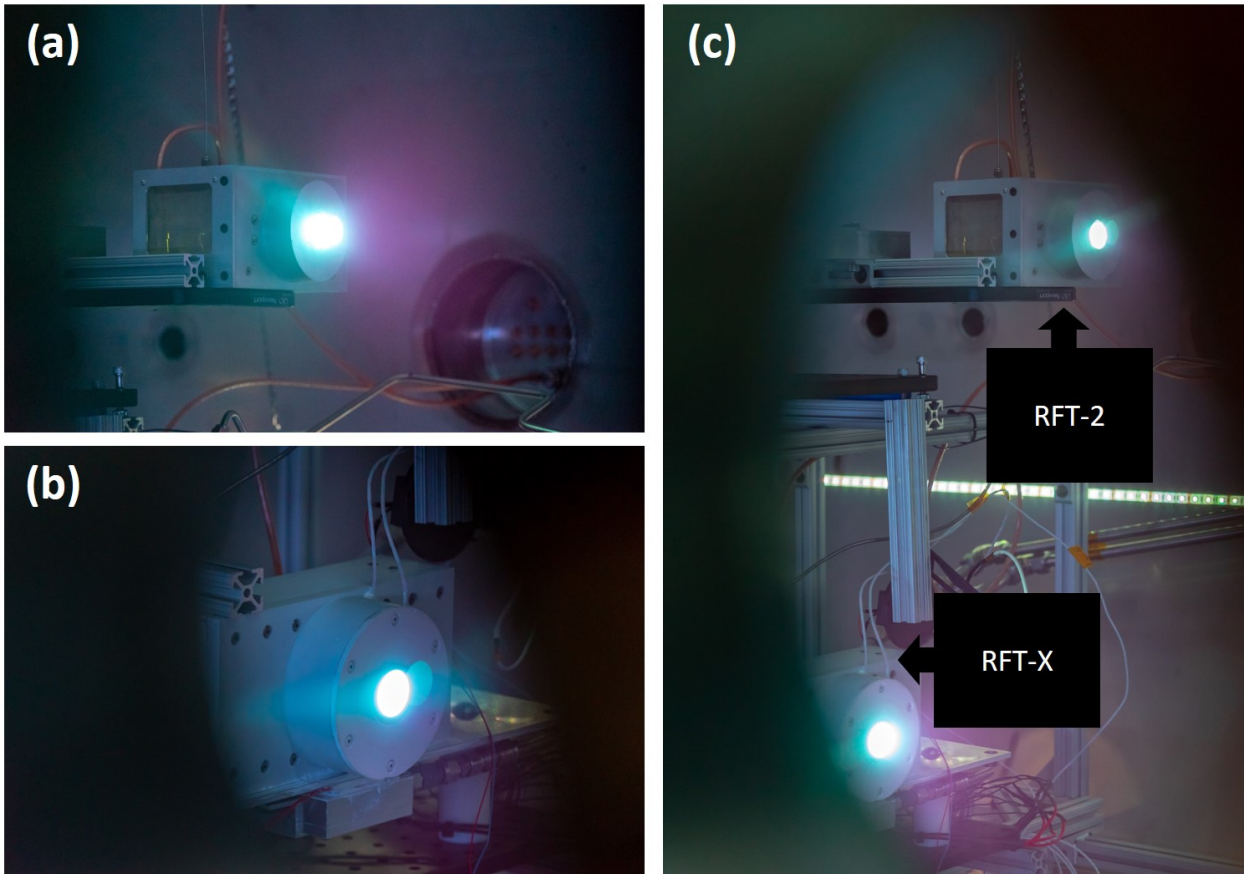

Fig. 2 Images of the RFT-2 firing at 100 W (a), RFT-X firing at 200 W (b) and both thrusters firing simultaneously (c) in the Phase Four Dreadnought vacuum facility with xenon propellant (10 sccm, each).

MHz to 2 GHz, was also placed in line for some measurements to calibrate the in line power meters. A proprietary match network was built into the thruster design, to maintain better than 95% power deposition in the thruster across the majority of operational points tested. Separately, an Alicat mass flow controller, with full scale resolution up to 50 sccm, provided gas flow to the engine. The uncertainty on the mass flow controller was ± 0.2 sccm. The complete thruster operational setup was controlled and monitored by custom software on the control computer. Phase Four's RFT control setup was designed to run up to two thrusters simultaneously, permitting the dual RFT-2/RFT-X firing image shown in Fig. 2c.

A. Vacuum Facilities

Experiments conducted were performed in Phase Four's large vacuum chamber, VCH-1 "Dreadnought", and at The Aerospace Corporation. A description of the facilities is provided here.

1. VCH-1 Dreadnought

Dreadnought consists of a 60" diameter by 96" long cylindrical stainless-steel vacuum chamber. Four Shiamadzu EI-V04M turbo-pumps provide 2100 L/s each of pumping on molecular nitrogen. All the turbo-pumps are backed in parallel by an Edwards IQDP80/QMB1200 which is also used to evacuate the chamber to the turbo-pumps' cross-over pressure of 30 mTorr. At pressures above 10^{-4} Torr, the chamber pressure is read by an IntruTech convection gauge. An IntruTech ion gauge mounted on top of the chamber is used at lower pressures. The VCH-1 system base pressure is 10^{-7} Torr after approximately 48 hours of pumping. Pressures reached during plasma production were between 1.7×10^{-5} and 2.3×10^{-5} Torr (calibrated for xenon) for mass flow rates between 3 and 10 sccm of xenon. A Stanford Research Systems residual gas analyzer (RGA) was also mounted on Dreadnought to actively monitor molecular weights of

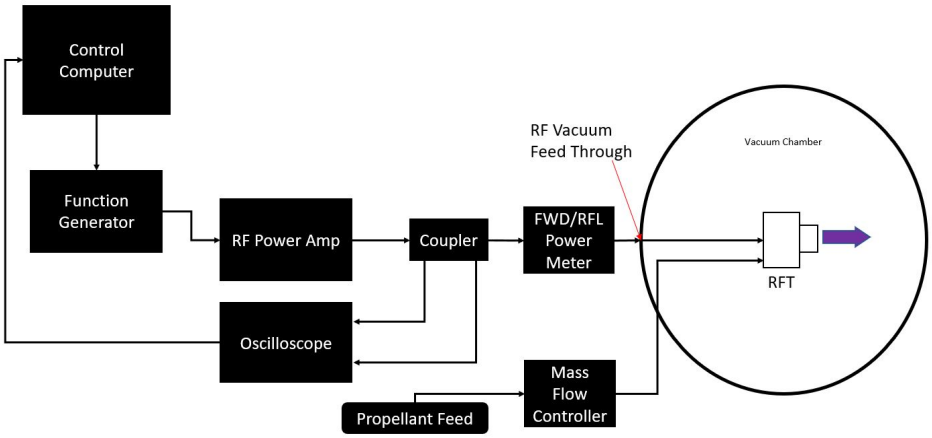

Fig. 3 A line diagram showing the main components of the RFT control and test setup.

constituents in the vacuum. The RGA was calibrated to the atomic weight and ionization energy of neutral molecular nitrogen. Figure 4 shows an image of Dreadnought and its pumping system.

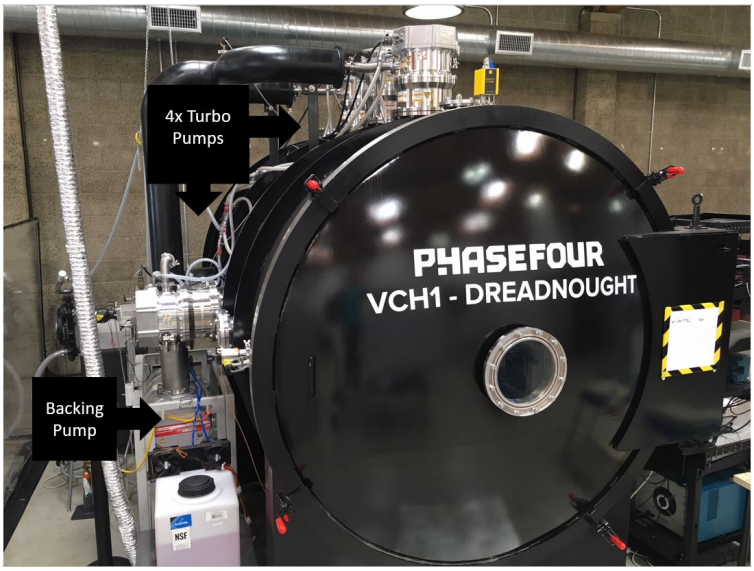

Fig. 4 An image of the VCH-1 Dreadnought vacuum facility showing the location of the pumps.

2. The Aerospace Corporation Vacuum Facility

The Aerospace Corporation operates an 86" diameter by 144" cylindrical vacuum chamber pumped by two 3,000 L/s Edwards STP-iXA3306 turbo-pumps and a 30,000 L/s Torrmaster TM900 cryopump. The vacuum chamber is brought to a rough vacuum with a Roots blower providing 12,690 L/s pumping speed and backed with eight 141 L/s Stokes 412 roughing pumps. For the measurements presented here, the base pressure was 9×10^{-8} Torr. Pressure in the vacuum chamber was monitored by a top-mounted hot-filament ion gauge.

B. Torsional Balance Thrust Stands

RFT-2 performance was measured at The Aerospace Corporation, and RFT-X was tested at Phase Four. In both cases, torsional balance thrust stands were used as the active diagnostic. The thrusters were placed on the end of the balance arm and mounted via an optical 1 inch bread board. The arm was balanced on a Riverhawk torsional spring

with factory calibrated spring constant. The thrust stand was balanced relative to the gravity vector using fine scale micrometer adjusted feet. The balance of the stand across the pivot point was achieved by placing counter weights on the other side of the arm as the thruster unit. A mirror was also placed on this end of the thrust stand, which was used as a target of an optical displacement sensor (ODS) to measure the motion of the arm during thruster operations. When the thruster fired, the thrust stand arm displaced a fixed distance as a function of the spring constant and the thrust output of the engine. Further details on the torsional balance design at The Aerospace Corporation are detailed elsewhere [8, 14].

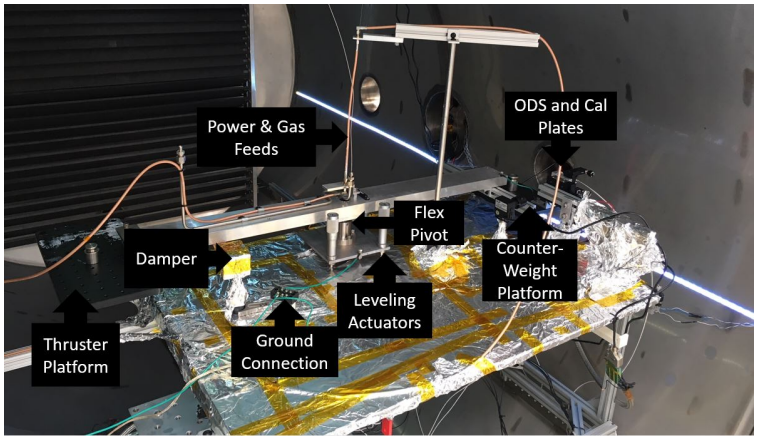

Fig. 5 An image of the Phase Four torsional balance thrust stand.

Figure 5 shows and image of Phase Four's torsional balance, which was modeled closely after the The Aerospace Corporation balance. After preliminary testing at higher RF powers it was determined that further accommodations were necessary to mitigate previously hidden effects at lower RF powers. Great lengths were taken to ensure a consistent ground plane underneath the thrust stand, and to maintain low resistance between the ground plane and the chamber ground. The thrust stand was damped using a single, electrically grounded eddy current damper (unlike the electrically floating dielectric fluid damper at The Aerospace Corporation). The damper resulted in a settling time of approximately 60 seconds. Contrary to measurements at The Aerospace Corporation, the power and fluid harnesses to the thruster were fed first to the thrust stand arm close to the pivot, and then along the arm to the thruster. This minimized any dynamic effects on the apparent spring constant by reducing the tension moment from the RF cable and gas feed line.

Like at The Aerospace Corporation, the Phase Four torsional balance was calibrated using a set of electrostatic plates on the opposite end of the arm as the thrusters. For a given voltage between the plates, the known force between them was used as a proxy for a thrust signal. The force between the plates for a given voltage and plate spacing was calibrated by a sensitive Ohaus mass scale. Thrust stand calibrations were performed before and after each test set while under vacuum, and up to 7 mN of force was applied between the electrodes. Details on this procedure are provided elsewhere [14].

The thrust stand was modeled as an underdamped simple harmonic oscillator. The oscillator natural frequency and damping constant were determined by comparing the thrust stand response to the known calibration plate forces. Subsequently, the response of the thrust stand to the thruster firing operations was recorded. To determine the thrust output, the thrust stand response was fit to an underdamped simple harmonic oscillator signal with the given natural frequency and damping constant from the calibrations, but with an unknown, time-varying thrust forcing function. Since regular, predictable drifts were present due to RF coaxial cable heating during operation, some post processing was necessary. The time scales for cable heating were much greater than the settling time of the thrust stand, therefore a linear correction fit was expected to be adequate to model the cable heating. To analyze a sample, a linear fit was applied to the calculated force function and was then subtracted from the raw data, providing a more accurate depiction of deflection due to thrust only. The change in deflection both at thruster off-on and thruster on-off was recorded to account for thrust stand and cable temperature changes. The on-to-off transition (marked by the black Δ arrow in Figure 6) was generally smaller than the on-to-off transition, and was also generally lesser than the linear shift over the course of a thrust fire. We hypothesize that this "residual" signal is caused by remaining warm gases out gassing from the plasma liner and gas feed lines after thruster shut off, though its exact source is still under investigation.

Uncertainties in the measurement were driven by uncertainties in the thrust stand spring constant and fit, uncertainties driven by thermal drifts, and uncertainties in calibration plate spacing. For the majority of measurements these combined

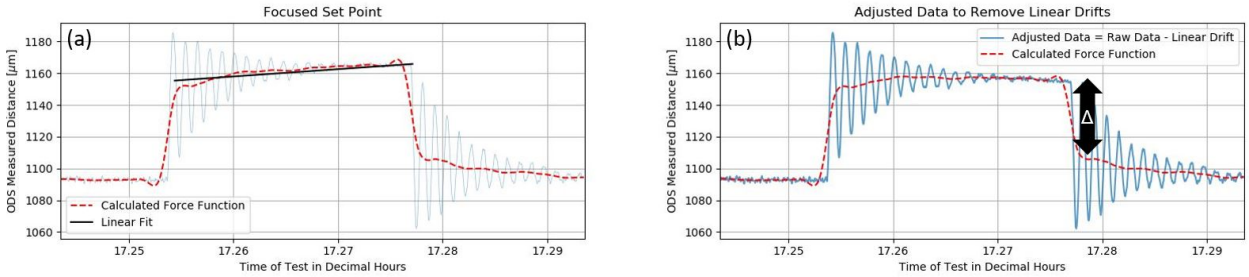

Fig. 6 An example of an RFT-X thrust stand response during a test operation. Test conditions were 7.5 sccm of xenon flow, at 234 W of RF power absorbed by the thruster. The on-to-off transition indicates an approximate thrust output of 3.8 mN.

to provide ≈ 10% error on the thrust measurements, however for a single set of high power data, a large drift in the thrust stand caused measurement uncertainties as high as 30%. These data are included in the set as their analysis along with the data with the lower uncertainty provide meaningful insight into the performance of the thrusters.

V. Results

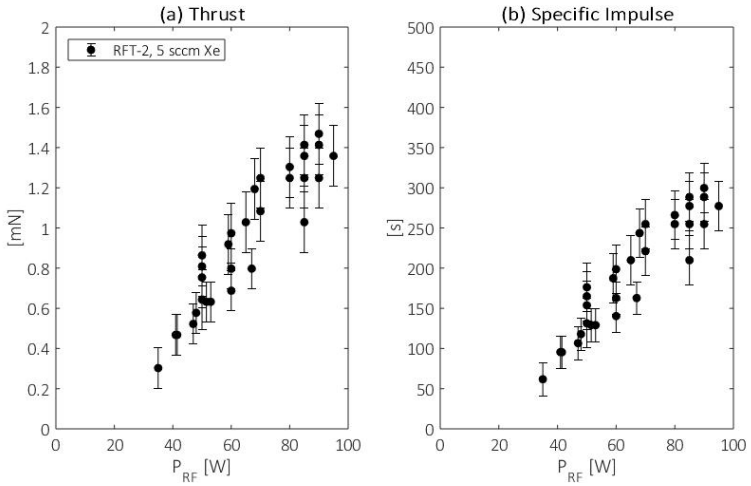

Fig. 7 Thrust and specific impulse data for RFT-2 between 35 W and 100 W of RF power, measured at The Aerospace Corporation.

Figure 7 shows thrust and specific impulse measurements of RFT-2 between 35 W and 100 W performed at The Aerospace Corporation. The RF power (P_{RF}) is the power absorbed by the plasma, calculated by the measured forward RF power minus the return power. Prior to plasma ignition, all of the power was reflected by the thruster back to the RF amplifier, confirming negligible stray RF absorption by the thruster. The thrust results include the displacement of the thrust stand due to cold gas and the plasma ignition. The peak performance observed at less than 100 W was 1.4 ± 0.2 mN, at 300 ± 50 seconds of specific impulse. At 95 W RF power, this yields a total thrust efficiency of approximately 2.1%. Specific impulse and thrust efficiency are defined as

$$I_{sp} = \frac{F_T}{\dot{m} g_0} \tag{1}$$

and

$$\eta = \frac{F_T^2}{2\dot{m} P_{RF}} \tag{2}$$

respectively, where $\dot{m}$ is the mass flow rate in kg/s, g_0 is the Earth's surface gravitational acceleration rate in m/s^2, F_T is the thrust of the engine in Newtons, and P_{RF} is the RF power into the thruster in Watts.

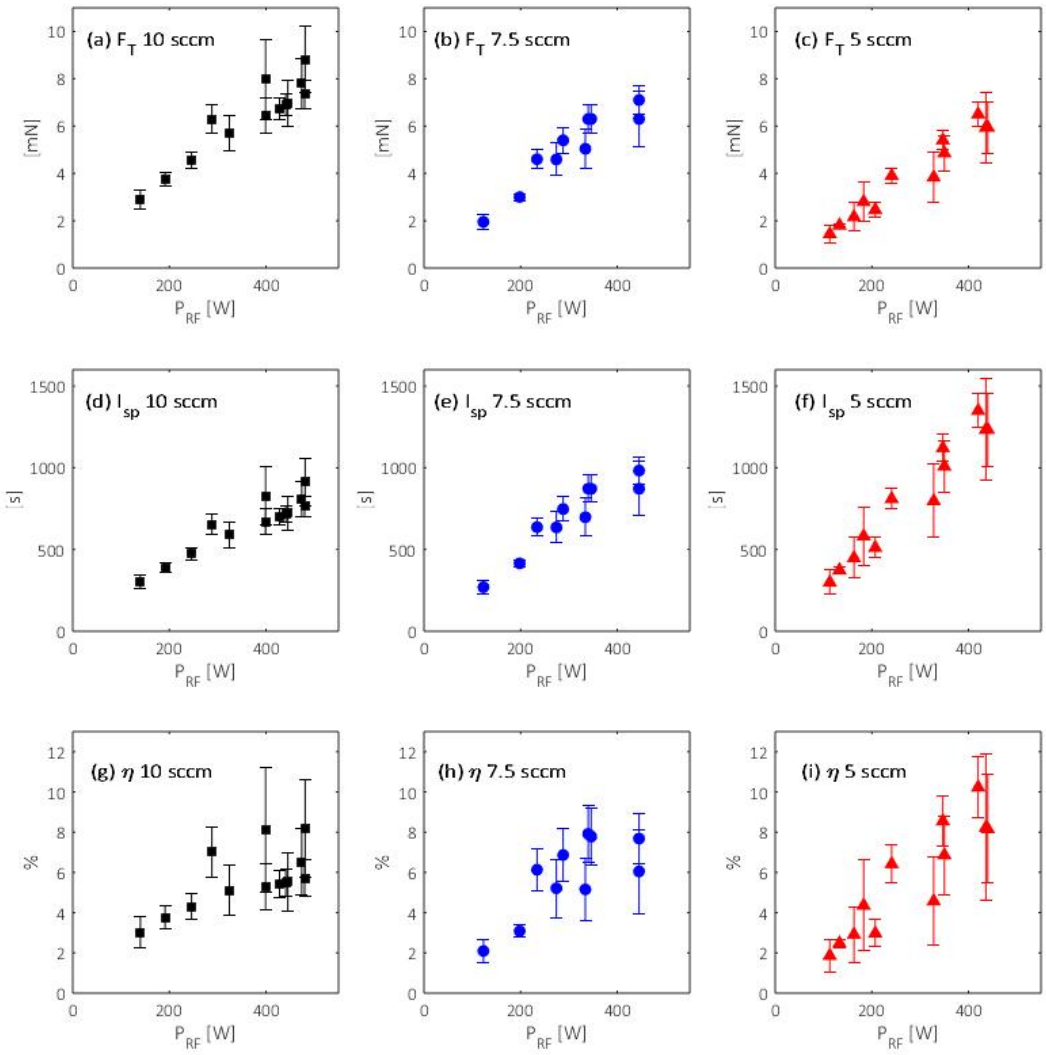

Fig. 8 Thrust (row 1), specific impulse (row 2), and efficiency data (row 3) for RFT-X across 10 sccm (column 1), 7.5 sccm (column 2), and 5 sccm (column 3) operating points.

Figure 8 shows RFT-X thrust, specific impulse, and thrust efficiency measurements performed at Phase Four between 100 W and 500 W of RF power, and at 5, 7.5 and 10 sccm of xenon flow. Two additional points were successfully tested at 3 sccm xenon flow, one at 99 W and one at 348 W. Those data are presented separately in the data summary set in Fig. 9. The 3 sccm data are not fully filled out because at that flow rate, the thruster was operating at the edge of its match network designed operating space. As such, only two discrete power operating points were found to be easily coupled to for the duration of a thrust measurement. The uncertainty on the RFT-X data varied between a few percent, to as much as 30% of the full scale thrust measurement. The points with large uncertainty were obtained when the RF power cable to the thrust stand was undergoing a significant change in drift rate, on top of its drift due to operational heating. Because of this, the linear subtraction of the cable heating drift shown in Fig. 6 provided a less accurate measurement of

the thrust signal. All the measurements with large error bars were obtained at set points where repeat shots were able to successfully demonstrate lesser uncertainty.

Similarly with the lower power RFT-2 unit, the performance scaled approximately linearly with input RF power. As expected, with lower mass flow rate, thrust decreased, but specific impulse and thrust efficiency increased. This suggests that ion acceleration increased disproportionally as mass flow decreased. Given that ion acceleration in such thrusters is driven by fast electrons ejected from the liner via the near-field RF signals, the results suggest that more efficient electron heating occurs at lower propellant flow rates, in accord with laboratory measurements [8, 15].

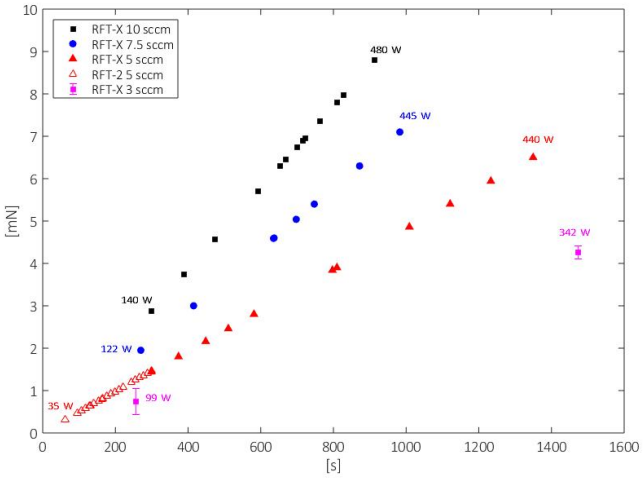

Fig. 9 Summary set of all performance data taken on RFT-2 and RFT-X using xenon propellant. All uncertainties are suppressed except for the 3 sccm data.

Figure 9 shows thrust versus specific impulse summary curves for all RFT-2 and RFT-X measurements across the full 35 W to 500 W power range. The set also includes the two successful measurements performed on RFT-X at 3 sccm. Besides these two data points, the uncertainty across all measurements is suppressed to clearly display the data. The minimum and maximum RF powers for each flow rate is written next to the relevant data point.

As discussed in the Introduction, the absence of electrodes in the Phase Four RFT allows for its use with novel, normally corrosive propellants. Among the new propellants of interest in the electric propulsion community is air, which aside from being much lower cost than xenon, is freely available for "low flying" satellites between 150 and 250 km of altitude. As an initial demonstration, the RFT-X unit was operated briefly on purely laboratory air plasmas, and the thrust and specific impulse was recorded. The RFT-X was able to consistently self-ignite and maintain the purely air plasma *without the need for any doping gas mixture*, such as argon or xenon, to aid in ionization. Figure 10 shows an image of the RFT-X firing with an air plasma at 400 W RF power, and Fig. 11 presents the resulting thrust and specific impulse data summary, overlaid on the xenon performance results from Fig. 9. As seen in the figure, thrust and specific impulse performance is poor compared to xenon at comparable mass flow rates and power, which is as expected for a higher ionization energy molecular propellant [16].

VI. Discussion

To the authors' knowledge, the specific impulse and thrust efficiency levels measured in the Phase Four RFT presented here represent the highest performance electrodeless thruster results ever demonstrated, by a significant margin. Specifically, the electrodeless RFT-X engine produced specific impulse on par with state of the art low power Hall effect thrusters, within 50% the thrust output at the same power level [17, 18]. This is as opposed to previous electrodeless thrusters that could not achieve the same order of magnitude thrust and/or specific impulse as their traditional Hall effect and gridded ion counterparts.

The performance improvement highlights improved understanding of the thruster ion acceleration and energy transfer mechanisms, which are captured in proprietary unified design rules that extend across thruster variants. The efficacy of these design rules are corroborated in Fig. 12. In this figure, both RFT-2 and RFT-X specific impulse data

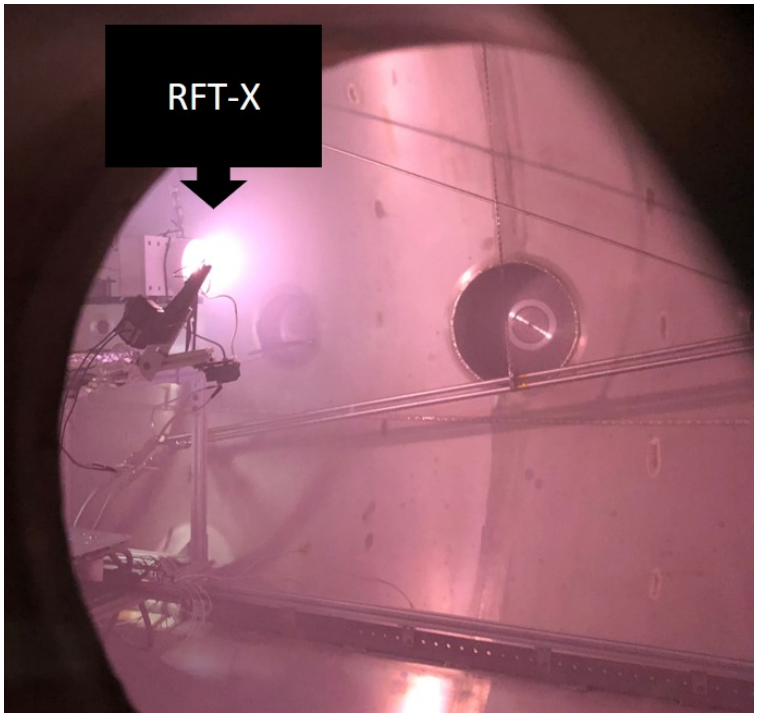

Fig. 10 An image of the RFT-X firing with an air plasma at 400 W input power.

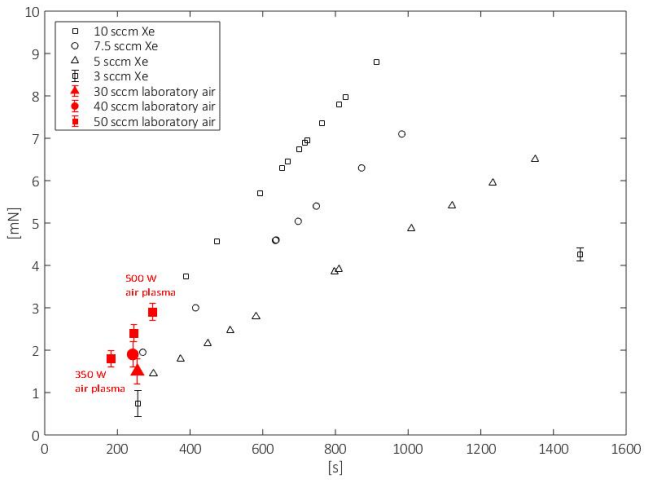

Fig. 11 Summary set of all performance data taken on RFT-X using xenon and air as propellant.

are overlaid, at 5 sccm xenon flow rate. RFT-2 was intended for less than 100 W RF power input, and RFT-X was intended to operate between 100 W and 500 W of input power. Both thrusters were designed with the common Phase Four RF thruster design rules. Despite the electrical, magnetic and mechanical differences between both thrusters, the specific impulse (and thus thrust, at the common mass flow rate) scaled according to the same linear trend. The common scaling suggests that the physical ion accelerating mechanisms between both systems are maintained despite the design variations between RFT-2 and RFT-X.

Another success of the RFT-2 and RFT-X test campaign is the exhibition of the flexibility of the thruster architecture. For the thrust measurements with air plasmas, the same RFT-X thruster with the same electrical matching network, magnetic and mechanical design, was used between xenon and air propellants. Another area where the RFT-X test

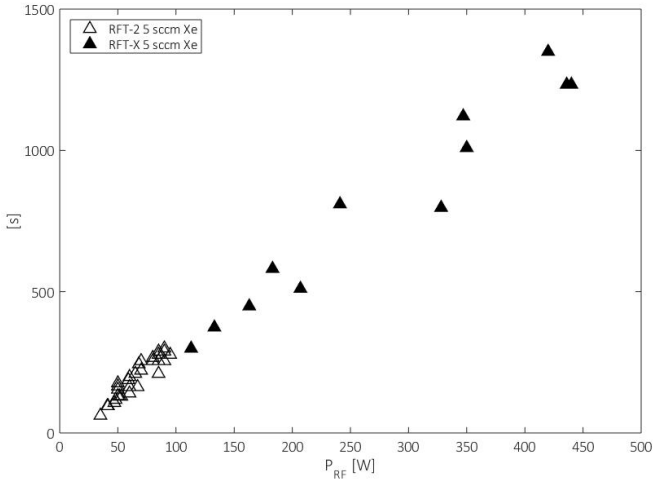

Fig. 12 Specific impulse produced by RFT-2 and RFT-X at 5 sccm xenon propellant flow versus input RF power.

thruster demonstrated flexibility, is in the wide range of thrust-specific impulse set points demonstrated for a common RF input power. As shown in Fig. 9, a single thruster was able to vary propellant flow input at a fixed power to achieve high thrust-low specific impulse, and high specific impulse-low thrust modes. Such a performance envelope is broader than the envelopes of comparable DC high voltage driven Hall effect and gridded ion thrusters commonly used today, which is caused by the differences in ion acceleration mechanism between RF electrodeless and DC thrusters.

Finally, all of the test thrusters used to present results here, were fabricated in the Phase Four prototype machine shop using basic computer controlled milling machines or simpler fabrication devices. The simplicity of the system, which permits its flexible application and ease of manufacturing, and the progress in performance presented here, show that electrodeless RF thrusters are rapidly maturing to meet the needs of the next generation of satellite constellations.

Acknowledgments

We thank Dr. Andrea Hsu, Dr. Rostislav Spektor and the team at The Aerospace Corporation for their help and advice on Phase Four's torsional balance thrust stand and measurement techniques. We also thank Dr. James Gilland from the Ohio Aerospace Institute for useful conversations on RF thrusters and the current state of the art in plasma propulsion.

References

[1] Khayms, V., and Martinez-Sanchez, M., "Design of a miniaturized Hall thruster for microsatellites," *AIAA, ASME, SAE, and ASEE, Joint Propulsion Conference and Exhibit*, AIAA, Buena Vista, FL, 1996.

[2] Rafalskyi, D., and Aanesland, A., "A Neutralizer-Free Gridded Ion Thruster Embedded Into A 1U Cubesat Module," *International Electric Propulsion Conference*, ERPS, Atlanta, GA, 2017.

[3] Leiter, H. J., Killinger, R., Bassner, H., Muller, J., and Kukies, R., "Development of the Radio Frequeny Ion Thruster RIT XT – A Status Report," *International Electric Propulsion Conference*, ERPS, Pasadena, CA, 2001.

[4] Squire, J. P., Chang-Diaz, F. R., Carter, M. D., Cassady, L. D., Chancery, W. J., Glover, T. W., Jacobson, V. T., McCaskill, G. E., Bengtson, R. D., Bering, E. A., and Deline, C. A., "High Power VASIMR Experiments using Deuterium, Neon and Argon," *International Electric Propulsion Conference*, ERPS, Florence, Italy, 2007.

[5] Charles, C., Takahashi, K., and Boswell, R. W., "Axial force imparted by a conical radiofrequency magneto-plasma thruster," *Applied Physics Letters*, Vol. 100, No. 113504, 2012. doi:10.1063/1.3694281.

[6] Williams, L. T., and Walker, M. L. R., "Thrust Measurements of a Radio Frequency Plasma Source," *Journal of Propulsion and Power*, Vol. 29, No. 3, 2013, pp. 520 – 527.

[7] Shabshelowitz, A., and Gallimore, A., "Performance and Probe Measurements of a Radio-Frequency Plasma Thruster," *Journal of Propulsion and Power*, Vol. 29, No. 4, 2013, pp. 919 – 929.

[8] Siddiqui, M. U., Cretel, C., Synowiec, J., Hsu, A. G., Young, J. A., and Spektor, R., "First Performance Measurements of the Phase Four RF Thruster," *International Electric Propulsion Conference*, ERPS, Atlanta, GA, 2017.

[9] Kinder, R. L., and Kushner, M. J., "Wave propagation and power deposition in magnetically enhanced inductively coupled and helicon plasma sources," *Journal of Vacuum Science and Technology, A*, Vol. 19, No. 1, 2001, pp. 76 – 86.

[10] Takahashi, K., Akahoshi, H., Charles, C., Boswell, R. W., and Ando, A., "High temperature electrons exhausted from rf plasma sources along a magnetic nozzle," *Physics of Plasmas*, Vol. 24, No. 084503, 2017.

[11] Chen, F. F., and Arnush, D., "Generalized theory of helicon waves. I. Normal modes," *Physics of Plasmas*, Vol. 4, No. 9, 1997.

[12] Kline, J. L., and Scime, E. E., "Parametric decay instabilities in the HELIX helicon plasma source," *Physics of Plasmas*, Vol. 10, No. 135, 2003.

[13] Chen, R. T. S., and Hershkowitz, N., "Multiple Electron Beams Generated by a Helicon Plasma Discharge," *Physical Review Letters*, Vol. 80, No. 21, 1998.

[14] Hsu Schouten, A., Beiting, E., and Curtiss, T., "Performance of a Torsional Thrust Stand with 1 μN Sensitivity," *International Electric Propulsion Conference*, ERPA, Kobe, Japan, 2015.

[15] Lafleur, T., Cannat, F., Jarrige, J., Elias, P. Q., and Packan, D., "Electron dynamics and ion acceleration in expanding-plasma thrusters," *Plasma Sources Science and Technology*, Vol. 24, No. 065013, 2015.

[16] Shabshelowitz, A., *Study of RF Plasma Technology Applied to Air-Breathing Electric Propulsion*, University of Michigan, Thesis, 2013.

[17] Frieman, J. D., Liu, T., Walker, M. L., Makela, J., Mathers, A., and Peterson, P. Y., "Performance Evaluation of the T-40 Low-Power Hall Current Thruster," *AIAA Propulsion and Energy Forum*, AIAA, Salt Lake City, UT, 2016.

[18] Conversano, R. W., Goebel, D. M., Hofer, R. R., Mikellides, I. G., and Wirz, R. E., "Performance Analysis of a Low-Power Magnetically Shielded Hall Thruster: Experiments," *Journal of Propulsion and Power*, Vol. 33, No. 4, 2017.